

# A Parametric Domain Map for Top Coat Damage Initiation and Propagation in EB-PVD Thermal Barrier Coatings

**Himanshu Bhatnagar, Mark E. Walter, & Somnath Ghosh**

*Department of Mechanical Engineering, The Ohio State University, Columbus, OH 43210, USA*

## ABSTRACT

---

*Despite providing superior protection of engine components from severe temperatures, thermal barrier coatings are susceptible to catastrophic failure due to large-scale interfacial delamination. Under operating conditions, interfacial waviness increases due to bond coat creep and the cyclic nature of the thermal loading. Recent analyses show that the top coat incurs cracks at the sites of interfacial undulation. The top coat cracks propagate and coalesce under cyclic thermal load, which leads to catastrophic interfacial delamination. In this article, a finite element model of the thermal barrier coating (TBC) system is developed in the commercial code ABAQUS to investigate dependencies on various parameters and to develop a simplified parametric understanding of the top coat crack initiation and propagation. A parametric domain map for assessing crack initiation and propagation is developed in terms of geometric parameters of the TBC. Thus the domain map identifies which TBC geometries yield a fail-safe design.*

---

\*Address all correspondence to ghosh.5@osu.edu

## 1. INTRODUCTION

The state-of-the-art electron beam physical vapor deposition (EB-PVD) thermal barrier coatings (TBCs) are used in gas turbine engines to protect components from high-temperature gases and severe transient thermal loading. As shown in the scanning electron microscope (SEM) micrograph of Fig. 1, a conventional TBC consists of three layers deposited on a superalloy substrate. The first layer is a 50- to 100- $\mu\text{m}$  thick bond coat that provides oxidation protection, while the second is a 100- to 120- $\mu\text{m}$  thick top coat for providing thermal insulation. The top coat is structured to be strain tolerant to avoid cracking and subsequent delamination; this is achieved by incorporating microcracks or aligned porosity in the material [1]. Typically, due to its low, temperature-insensitive thermal conductivity [1], Yttria-stabilized Zirconia (YSZ) is the material of choice for the top coat. The top coat is transparent to oxygen, and thus a third layer, the thermally grown oxide (TGO), forms as the bond coat oxidizes. Owing to TGO growth and the creep deformation of the bond coat, the morphology of the interfaces between TGO and adjoining layers continue to evolve during the life of the TBC [2]. As shown in Fig. 1, the SEM images of the TBC microstructure reveal that the TGO interfaces may be planar or wavy.

Individual layers in TBCs are significantly stronger than the interfaces between the top coat

and TGO and between the TGO and bond coat. Furthermore, the interface toughness also tends to degrade with exposure time [4]. Consequently, over their service life, TBCs are susceptible to delamination along the top and/or bottom TGO interfaces. Thus modeling the delamination phenomena is of considerable interest to the engineering community.

Experimental observations [2,5] confirm that in the absence of significant bond coat creep, delamination is predominantly along the TGO and bond coat interface. TBC spallation is preceded by a competition between buckling and interface delamination that is stimulated by the waviness of the interface. The competing mechanisms have been extensively investigated in the literature [6–9] and were recently formalized parametrically to enable identification of the dominant failure mechanism for TGO and bond coat delamination [9].

There is also evidence that with significant bond coat creep, damage initiates within the top coat, leading to delamination of the top coat and TGO interface [10–12]. Damage within the top coat is primarily driven by the stresses developed due to the coefficient of thermal expansion (CTE) mismatch between the different layers during thermal loading as well as by creep deformation of the bond coat. A number of geometrical and mechanical factors are known to contribute to the damage initiation and propagation within the top coat. Notable among these are important geometric and morphological features of interfaces and constituent layers and their thermomechanical properties.

A significant body of work exists in the literature characterizing the growth of undulations under cyclic loading [10–12]. A number of these investigations also consider the top coat damage [11,12], but the relationship between damage and geometric and material factors has not been addressed in detail. Xu et al. [13] have demonstrated the variation in energy release rate as the crack propagates within the top coat for crack paths that were selected a priori.

This article is aimed at the development of parametric domain maps delineating safer TBC system designs from those prone to failure. The multi-dimensional parametric space is represented as a reduced-order two-dimensional parametric domain map for the crack initiation in terms of the critical geometric parameters. This map is created through parametric finite element simulations that

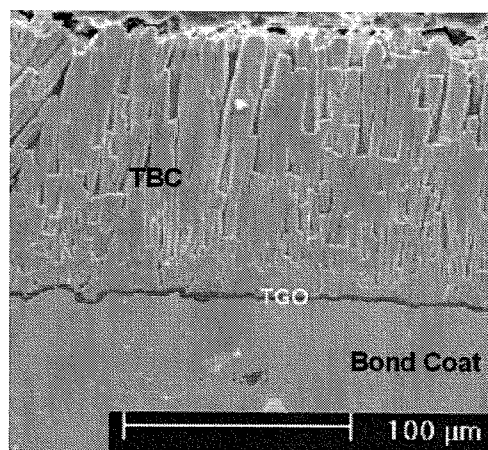


**FIGURE 1.** An SEM image of the thermal barrier coating (TBC) microstructure consisting of the top coat, the thermally grown oxide layer, the bond coat, and the super-alloy substrate [3]

include the substrate, bond coat, TGO, and top coat. The crack path is not postulated a priori; instead, crack initiation and its subsequent trajectory is determined based on the local drivers at the crack tip. A sensitivity analysis is employed to first estimate the contribution of material and geometric parameters to crack initiation. Subsequently, sensitivities to parameters responsible for crack initiation are investigated through crack propagation simulated with a hysteretic cohesive zone model.

The development of a domain map enables the realization and selection of geometric parameters that result in a safer TBC. As a final step, based on the predictions of the parametric domain map, which incorporates crack initiation followed by crack propagation, two representative failure scenarios are simulated. The geometry and material properties for these cases are obtained from the literature, and the predicted crack trajectories are found to be in good agreement with experimental observations in the literature [2,7]. The models developed in this article are micromechanical in nature, with explicit damage representation at the micromechanical scale of the TBC. However, the implications of the model are macroscopic in that it is used to predict overall reliability of EB-PVD TBCs.

## 2. THE TOP COAT FAILURE MECHANISMS AND SOLUTION APPROACH

In the context of linear elasticity, TBCs are insensitive to cyclic loading, and the failure mechanisms are limited to TGO interfaces [6–8]. However, incorporating bond coat creep introduces significant nonlinearity to the TBC response under cyclic loading and also activates an alternate failure mechanism reported by Evans et al. [7] and Karlsson et al. [12]. During operation under cyclic thermal loads, the TBC can experience critical loads, causing crack initiation within the top coat and at the site of interfacial undulations. During subsequent cycles of loading, the initial crack may (1) propagate until it reaches the interface, (2) propagate away from the interface, or (3) be arrested without any subsequent propagation. The probability of crack initiation and its eventual trajectory in a TBC under operating conditions will depend on various geometric and material parameters as well as the applied loading. Hence it is of interest to study the influence of TBC parameters on initiation and propagation of

top coat cracks. A brief introduction to the methods used to study the initiation and propagation of cracks is presented next.

### 2.1 Crack Initiation within the Top Coat

In addition to significant in-plane compressive stresses caused by its thermal expansion mismatch with the substrate, the top coat is also subjected to out-of-plane tensile stresses due to the wavy morphology of the top coat and TGO interface. This renders the top coat susceptible to cracking in the vicinity of interfacial undulations. Since the material of choice is brittle YSZ, the top coat cracking is likely to initiate in mode I. A mode I crack initiation criterion similar to [14] is employed, where damage appears as a finite crack oriented normal to principal direction, when, as given in Eq. (1), the maximum of first principal stress ( $S1^{\max}$ ) exceeds rupture stress ( $\sigma_{\text{rupture}}$ ):

$$S1^{\max} \geq \sigma_{\text{rupture}} \quad (1)$$

Crack initiation is sensitive to the rupture stress rather than fracture energy; hence, even though the top coat and TGO interface toughness is lower than the bulk top coat, the rupture stress is assumed to be invariant. It enables identification of safer TBC designs through a sensitivity analysis to determine the relationship of  $S1^{\max}$  to various geometric and material parameters. The parameters considered for this study are shown pictorially in Fig. 2 and include (1) top coat modulus  $E_{\text{TC}}$ , (2) TGO modulus  $E_{\text{TGO}}$ , (3) TGO thickness  $h$ , (4) amplitude  $A$  and wavelength  $W$  of the undulation, and (5) thermal cycle parameters, including peak temperature and heating, holding, and cooling time. Since the resulting crack is oriented normal to the principal direction for mode I fracture, the orientation of the principal axis is recorded so that propagation of a nascent crack can be studied.

### 2.2 Propagation of Cracks Originating within the Top Coat

The top coat may incur cracks due to local tensile stresses at the sites of interfacial undulations, however, not all cracks will contribute to the large-scale failure of TBC. The critical cracks that require further investigation are those that propagate with each load cycle and reach the interface. Since the

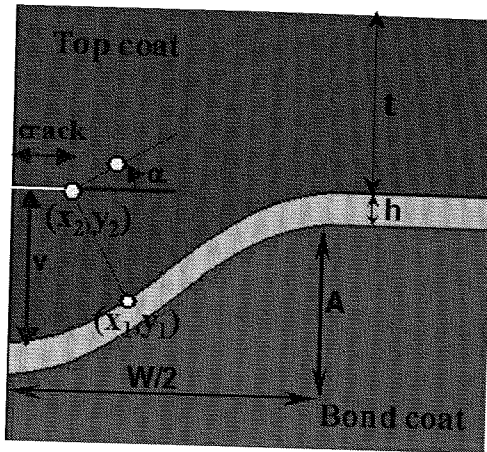


**FIGURE 2.** Schematic of the TBC model showing geometric and dimensional parameters of the undulation as well as the location of the crack characterized by normal distance  $v$ . The substrate, excluded here for clarity, is included in the finite element model

cracks that reach the interface will initiate delaminations, it is of interest to understand their sensitivity to the various parameters. In recent years, cohesive zone models have emerged as important tools for modeling crack propagation in homogeneous and heterogeneous materials [15–19]. Cracking is simulated by inserting special cohesive elements between continuum elements (e.g., [15,17,19]). The use of a highly refined computational mesh, especially near the crack tip, is also a requirement, even though the effect is mitigated due to the finite crack tip stresses provided by the cohesive zone. In this article, a state-of-the-art cohesive zone model is employed along with a criterion for crack path evolution determined by the local crack tip state, thus eliminating the mesh-dependent prediction of the crack path, even with a structured mesh. These computational tools are described in the next two subsections.

### 2.2.1 Hysteretic Mixed-Mode Cohesive Element Formulation

Owing to the cyclic nature of the thermal loading, TBCs may incur significant fatigue damage within the top coat, leading to crack coalescence and failure. The hysteretic cohesive models proposed by Nguyen et al. [20] and Maiti and Guebelle [21] are found to be suitable for such failure, but they

are limited to mode I loading. Although top coat cracks are assumed to initiate under mode I loading, they may experience mixed-mode loading as they extend along complicated trajectories. Hence, for TBC application, a hysteretic cohesive model is extended to mixed-mode loading that reduces to an irreversible bilinear, rate-independent cohesive law under monotonic loading [18,21].

The bilinear cohesive model is discussed in detail elsewhere (e.g., [18]) and is summarized by the following traction separation law:

$$T = \begin{cases} \frac{\sigma_{\max}}{\delta_c} \delta & \text{if } \delta < \delta_c \text{ (hardening region)} \\ \frac{\sigma_{\max}}{\delta_c - \delta_e} (\delta - \delta_e) & \text{if } \delta_c < \delta < \delta_e \\ & \text{(softening region)} \\ 0 & \text{if } \delta > \delta_e \text{ (completely debonded)} \end{cases} \quad (2)$$

The effective separation and effective traction are defined as  $\delta = \sqrt{\delta_n^2 + \beta^2 \delta_t^2}$  and  $T = \sqrt{T_n^2 + \beta^{-2} T_t^2}$ , respectively, where  $\delta_n$  and  $T_n$  are the normal separation and traction,  $\delta_t$  and  $T_t$  are the tangential separation and traction, and  $\beta$  is an empirical factor. As the effective separation increases, the effective traction reaches a maximum value ( $\sigma_{\max}$ ) at  $\delta_c$  and then decreases for further increase in separation. This increase in traction is known as hardening. The subsequent decrease is known as softening, which introduces irreversibility through monotonic decay of the peak stress due to damage. At a selected effective separation ( $\delta_e$ ), the tractions vanish, indicating the failure of the element.

Regardless of whether the element is in the hardening or softening region, the unloading is always assumed to be toward the origin of the traction separation curve. Thus the bilinear cohesive model remains fully reversible within the hardening region. Once it enters the softening region ( $\delta \geq \delta_c$ ), any subsequent unload/reload occurs with reduced stiffness, rendering the deformation irreversible. On reloading, it returns to the state at the beginning of unload, and additional monotonic damage can be accrued on further loading.

To account for dissipative mechanisms in the fracture process zone ahead of the crack tip, a hysteretic model incurs fatigue damage only during reloading. This damage can occur at any point, including when the element is in the so-called hardening region. Unloading is still assumed to be linearly

toward the origin of the traction separation curve, and therefore hysteresis curves are formed. During reloading, the stiffness of the cohesive element is assumed to decay according to the stiffness degradation given in Eq. (3). The rate of stiffness decay is controlled by the introduction of an additional parameter  $\delta_f$ :

$$\begin{aligned} \dot{K}_{nn} &= \begin{cases} -K_{nn}^p \frac{\dot{\delta}_n}{\delta_f} & \text{if } \dot{\delta}_n > 0 \\ 0 & \text{if } \dot{\delta}_n \leq 0 \end{cases} \\ \dot{K}_{tt} &= \begin{cases} -K_{tt}^p \frac{\dot{\delta}_t}{\delta_f} & \text{if } \dot{\delta}_t > 0 \\ 0 & \text{if } \dot{\delta}_t \leq 0 \end{cases} \end{aligned} \quad (3)$$

These incremental stiffness equations are converted to difference equations to calculate the stiffness at the  $(p+1)$ th step based on the stiffness of the  $p$ th load step and increment in displacement jump. The resulting normal and tangential stiffnesses are

$$K_{nn}^{p+1} = K_{nn}^p e^{-\frac{\Delta\delta_n}{\delta_f}} \quad \text{where } \Delta\delta_n = \delta_n^{p+1} - \delta_n^p \quad (4)$$

$$K_{tt}^{p+1} = K_{tt}^p e^{-\frac{\Delta\delta_t}{\delta_f}} \quad \text{where } \Delta\delta_t = \delta_t^{p+1} - \delta_t^p$$

Owing to the incremental nature of fatigue damage, increments in normal and tangential tractions are calculated using the following equation:

$$\begin{pmatrix} \dot{T}_n \\ \dot{T}_t \end{pmatrix} = \begin{bmatrix} K_{nn} & 0 \\ 0 & K_{tt} \end{bmatrix} \begin{pmatrix} \dot{\delta}_n \\ \dot{\delta}_t \end{pmatrix} \quad (5)$$

Using the backward Euler method, the normal and tangential tractions at the  $(p+1)$ th step are evaluated using the updated stiffness, as given in Eq. (6):

$$\begin{aligned} T_n^{p+1} &= T_n^p + K_{nn}^{p+1} \Delta\delta_n \\ T_t^{p+1} &= T_t^p + K_{tt}^{p+1} \Delta\delta_t \end{aligned} \quad (6)$$

The hysteretic response of the cohesive model remains within the envelope of the bilinear model, and when the reloading curve intersects the softening curve, it follows the curve for as long as the loading process continues. During such periods, the element accrues only monotonic damage, without any fatigue damage. From the above formulation, it can be seen that five cohesive zone parameters, namely,  $\sigma_{\max}$ ,  $\delta_c$ ,  $\delta_e$ ,  $\delta_f$ , and  $\beta$ , define the hysteretic cohesive zone response. Figure 3 graphically illustrates the traction separation response of the hysteretic cohesive model under cyclic loading.

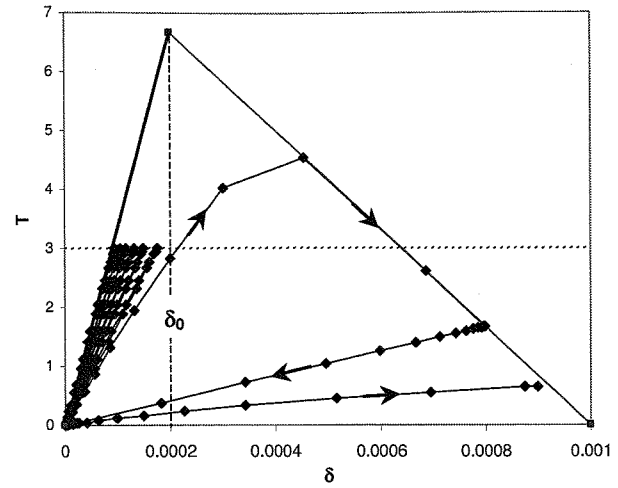


FIGURE 3. A plot showing the hysteretic cohesive zone element response with cyclic loading to eventual failure when  $\delta = \delta_e = 0.001$

### 2.2.2 Incremental Direction of Crack Propagation

The crack trajectory cannot be determined a priori as it depends on the local drivers at the crack tip. This makes it imperative to evaluate the direction of crack propagation at each increment of loading, as the crack is restricted to follow the trajectory defined by the cohesive zone elements. The following are among the numerous methods proposed in the literature to evaluate incremental direction: the maximum circumferential stress  $\sigma_{\theta\theta}^{\max}$  criterion [22], the maximum energy release rate criterion [23], and the strain energy density criterion [24]. In this work, direction is determined using the maximum cohesive energy criterion proposed by Li and Ghosh [16]. This criterion postulates that the crack will propagate in the direction that maximizes the available cohesive energy. From the definition of the  $J$ -integral, a relation between the cohesive energy  $\phi$  for complete decohesion and the critical energy release rate  $G_c$  has been established in [17] as

$$G_c = J = \int_0^R T \frac{\partial \delta}{\partial x} dx = \int_0^{\delta_c} T d\delta = \phi \quad (7)$$

where  $R$  is the length of the cohesive zone. Consequently, for a given crack tip state of stress, the crack growth direction is estimated as that along which  $G_c$ , or equivalently, the cohesive energy  $\phi$ , is maximized. The cohesive energy  $\phi_A$  at the crack tip  $A$



along any direction  $\alpha$  can be expressed for an arbitrary effective separation  $\delta(\alpha)$  as

$$\phi_A(\alpha) = \left( \int_0^{\delta(\alpha)} T(\alpha) d\delta \right)_A = \left( \int_0^{t(\alpha)} T(\alpha) \cdot \frac{\partial \delta}{\partial t} dt \right)_A \quad (8)$$

where  $T(\alpha) = \sqrt{(T_n^{\text{coh}})^2 + \beta^{-2} (T_t^{\text{coh}})^2}$  is the magnitude of the effective cohesive traction. The corresponding unit normal  $\mathbf{n}$  and tangential  $\mathbf{t}$  vectors along the direction  $\alpha$  are expressed as

$$\mathbf{n} = -(\sin \alpha)\mathbf{i} + (\cos \alpha)\mathbf{j} \quad \mathbf{t} = (\cos \alpha)\mathbf{i} + (\sin \alpha)\mathbf{j} \quad (9)$$

The normal and tangential components of the cohesive traction force at an angle  $\alpha$  are then deduced as

$$\begin{aligned} \begin{Bmatrix} T_n^{\text{coh}} \\ T_t^{\text{coh}} \end{Bmatrix} &= \begin{bmatrix} n_x & n_y \\ t_x & t_y \end{bmatrix} \begin{Bmatrix} \sigma_{xx}n_x + \sigma_{xy}n_y \\ \sigma_{xy}n_x + \sigma_{yy}n_y \end{Bmatrix} \\ &= \begin{Bmatrix} \sigma_{xx} \sin^2 \alpha + \sigma_{xy} \sin 2\alpha + \sigma_{yy} \cos^2 \alpha \\ -\frac{1}{2} \sigma_{xx} \sin 2\alpha + \sigma_{xy} \cos 2\alpha + \frac{1}{2} \sigma_{yy} \sin 2\alpha \end{Bmatrix} \quad (10) \end{aligned}$$

and hence the effective cohesive traction for direction  $\alpha$  is

$$T(\alpha) = \sqrt{\begin{aligned} &(\sigma_{xx} \sin^2 \alpha - \sigma_{xy} \sin 2\alpha + \sigma_{yy} \cos^2 \alpha)^2 \\ &+ \beta^{-2} \left( -\frac{1}{2} \sigma_{xx} \sin 2\alpha + \sigma_{xy} \cos 2\alpha + \frac{1}{2} \sigma_{yy} \sin 2\alpha \right)^2 \end{aligned}} \quad (11)$$

The incremental direction of crack propagation is assumed to maximize the cohesive energy at  $A$ , according to the criteria

$$\frac{\partial \phi_A(\alpha)}{\partial \alpha} = 0 \quad \frac{\partial^2 \phi_A(\alpha)}{\partial \alpha^2} < 0 \quad (12)$$

The resulting direction of crack propagation  $\alpha_0$  is obtained by inserting Eq. (11) into Eq. (8) and using the maxima criteria in Eq. (12) and can be written as follows:

$$\begin{aligned} \alpha_0 &= \sin^{-1} \left( \left[ \sigma_{yy} - \sigma_{xx} \pm \sqrt{(\sigma_{xx} - \sigma_{yy})^2 + 4\sigma_{xy}^2} \right] \right. \\ &\quad \left. \sqrt{\left( \sigma_{yy} - \sigma_{xx} \pm \sqrt{(\sigma_{xx} - \sigma_{yy})^2 + 4\sigma_{xy}^2} \right)^2 + 4\sigma_{xy}^2} \right) \quad (13) \end{aligned}$$

The change in crack trajectory is achieved by generating a new mesh incorporating an updated crack

path laced with cohesive elements. To reduce the computational expense associated with this process, the crack trajectory update is subjected to a geometric criterion that identifies whether there are tendencies for significant directional variation. The proposed geometric criterion requires that the crack path be updated only when the incremental direction ( $\alpha_0$ ) exceeds a tolerance limit based on the critical angle ( $\alpha_c$ ) that minimizes the crack tip distance to the interface. Figure 2 illustrates the crack geometry and critical angle pictorially. As the undulation is idealized with a sinusoidal wave, represented in Eq. (14a), and the critical angle corresponds to the normal from the crack tip ( $x_2, y_2$ ) to the interface ( $x_1, y_1$ ),  $\alpha_c$  can be determined using the trigonometric relation in Eq. (14b) and is given in Eq. (15):

$$y_1 = -A \left( 1 + \sin \left( \frac{\pi}{2} - \frac{x_1}{W} \pi \right) \right) \quad (14a)$$

$$\frac{y_2 - y_1}{x_2 - x_1} = - \left( \frac{dy_1}{dx_1} \right)^{-1} = - \frac{W}{\pi A \cos \left( \frac{\pi}{2} - \frac{x_1}{W} \pi \right)} \quad (14b)$$

$$\alpha_c = \tan^{-1} \left( \frac{y_2 - y_1}{x_2 - x_1} \right) \quad (15)$$

Equation (15) shows that the critical angle of propagation is a function of crack tip location and the undulation geometry. The crack path is updated when  $\|\alpha_0\|/\|\alpha_c\|$  is greater than 0.1%.

### 3. FINITE ELEMENT MODELS OF THERMAL BARRIER COATING

#### 3.1 Material Models

Advanced TBCs typically have nickel-based superalloy substrates with high strength and stiffness, even at elevated temperatures. The bond coat material of choice is an intermetallic platinum modified nickel aluminide with a CTE similar to that of the substrate material. Mechanical properties of the bond coat material may vary with thermal cycling, and the bond coat may also undergo significant creep deformation at elevated temperature [25]. A thermally activated creep material model for the bond coat has been proposed in [25] based on microtensile test results performed on bond coats extracted from actual TBC systems. The model is phenomenological in nature and does not account for explicit variables at the microstructural level. The strain rate stress law in this model is expressed as

$$\begin{aligned}\dot{\epsilon}_{\text{creep}} &= 7.5 \times 10^{20} \left(\frac{\sigma}{E}\right)^{2.7} \exp\left(\frac{-340 \text{ [kJ/mol]}}{RT}\right) \\ T &< 800^\circ\text{C} \\ \dot{\epsilon}_{\text{creep}} &= 9.1 \times 10^{27} \left(\frac{\sigma}{E}\right)^4 \exp\left(\frac{-400 \text{ [kJ/mol]}}{RT}\right) \\ T &> 800^\circ\text{C}\end{aligned}\quad (16)$$

where  $\dot{\epsilon}_{\text{creep}}$  is the equivalent creep strain rate,  $\sigma$  is the equivalent deviatoric stress,  $R$  is the gas constant, and  $T$  is the absolute temperature. The model was calibrated with experiments in [25], and a change in model parameters was found at  $800^\circ\text{C}$ . This bond coat material model is implemented as a user subroutine in the ABAQUS [26] finite element package.

The effect of bond coat creep on the out-of-plane creep strain accumulation in the bond coat has been investigated analytically by Balint and Hutchinson [27] and numerically by Karlsson et al. [12]. Numerical implementation of the creep material model in this study is validated through reproducing results reported in [25] with similar geometry and material properties.

Although it is believed that damage initiates in the top coat [2] and accurate material models of the top coat are essential, the YSZ with a strain-tolerant columnar structure is not well characterized in the literature. The effect of the top coat material model was investigated to determine the best representation for accurate prediction of failure. The thermal expansion coefficient of the TGO is less than that of the substrate, causing very high compressive stresses in the TGO. The TGO reduces these stresses by lengthening through out-of-plane displacements that increase the undulations accommodated by a relatively compliant bond coat [11]. However, the top coat provides a constraint that restricts such deformation and leads to out-of-plane stresses near the undulations. The magnitude and location of these stresses clearly depend on the top coat stiffness. A compliant top coat would not restrict TGO deformation, and the out-of-plane stresses would localize at the TGO and top coat interface due to bending of the TGO. However, a stiffer top coat will prevent TGO deformation, resulting in out-of-plane tensile stresses in the vicinity of the undulation. Since experimental observations in [2,7,13] suggest that cracks initiate away from the interface at the undulation sites, the top coat is idealized as an isotropic elastic material with no preexisting

flaws. Furthermore, although the columnar structure of the top coat suggests that under tension, it will be more compliant in plane than out of plane, CTE mismatches between the top coat and substrate will lead to in-plane compression. With little in-plane tension during load, effects of the columnar microstructure should not be significant. Mechanical properties of the top coat are sensitive to deposition process parameters as well as to the intercolumnar spacing [28]. The properties may also vary during the TBC service life due to sintering [29] with total exposure time at high temperatures. However, this variation is not significant over individual thermal cycles. Solutions with four different top coat moduli, ranging between 100 and 220 GPa, are considered in this study to account for microstructure variability in the specimens. Table 1 presents material property values for each of the TBC layers obtained from those reported by Evans et al. [7] and Cheng et al. [30]. The rupture stress for the top coat is assumed to be same as homogeneous YSZ reported in [31].

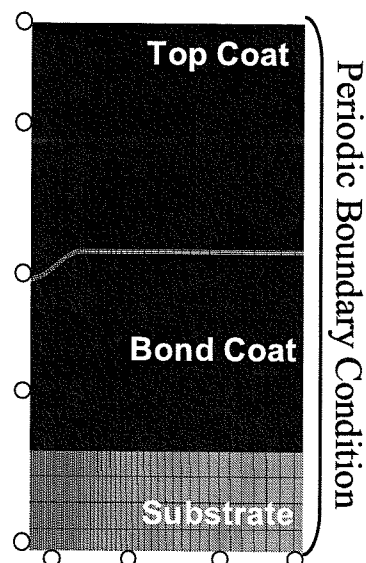
### 3.2 Geometric Model and Finite Element Mesh

A finite element model of the TBC system, including the substrate, bond coat, TGO, and top coat, is shown in Fig. 4. Two-dimensional plane strain representations of the TBC system are selected as undulations and are assumed to run through the sample thickness. The TBC morphology is assumed to be symmetric about the vertical plane, and only the half geometry is modeled. From Fig. 1, it can be observed that undulations in the vicinity of planar interfaces between the TGO and bond coat are commonly observed due to the initial and growing surface roughness of the bond coat. In this study, only sinusoidal undulations penetrating into the bond coat are considered.

A  $150 \times 1100 \mu\text{m}$  section of the TBC system is modeled with a graded mesh of four-noded elements, which are identified as CPE4(QUAD2D) in the ABAQUS element library [26]. The resulting model consists of more than 11,000 elements and 12,000 nodes and exhibits less than 0.5% error in the strain energy when compared to a more refined mesh. As shown in Fig. 4, a highly refined mesh is used in the vicinity of the TGO undulation, and the mesh becomes coarse away from the region of interest.

**TABLE 1.** Material properties of components of the TBC system as obtained from [7,30,31]

Property	Substrate	TGO	TBC
Poisson's ratio	0.31–0.35	0.23–0.25	0.10–0.12
Elastic modulus (GPa)	120–220	320–400	100–220
Thermal expansion coefficient ( $10^{-6}/^{\circ}\text{C}$ )	14.8–18.0	4.0–8.0	6.0–12.2
Rupture stress (Mpa)	–	–	287

**FIGURE 4.** Finite element model (*not to scale*) of the TBC system, with the bottom of substrate constrained to remain flat, symmetry at the left vertical edge, and radial periodicity at the right vertical edge

### 3.3 Boundary Conditions

In practice, the top surface of the TBC is exposed to hot combustion gases and is assumed to be free of any mechanical constraints or loads. The current TBC system model is subjected to a cyclic thermal load through variation of a uniformly applied temperature from  $1000^{\circ}\text{C}$  to room temperature of  $30^{\circ}\text{C}$ . Each nominal temperature cycle includes 10-min heating, 10-min hold at peak temperature, and 10-min cooling. All analyses are performed for five successive cycles. The thermal loads caused by this thermal cycle generate in-plane compressive stresses in the TGO and top coat on account of the CTE mismatch. Although temperature gradients are expected along the TBC thickness during service, the uniform thermal load assumption is considered adequate since out-of-plane thermal

effects are secondary to undulation stresses. For all analyses, symmetry boundary conditions are applied at the left edge; a rigid substrate is simulated, with roller supports applied at the lower horizontal boundary; and radial periodic boundary conditions are applied at the right edge of the models. These boundary conditions are shown pictorially in Fig. 4.

### 3.4 Cohesive Zone Element Implementation

The hysteretic cohesive model described in Section 2.2 is implemented as a four-noded cohesive element within ABAQUS's user-defined element subroutines [26]. These elements are compatible with the regular, continuum ABAQUS QUAD2D elements. The element comprises two cohesive surfaces with two nodes each. In the initial, unloaded state, the nodes of the two surfaces share the same coordinates. With the application of external load, the surfaces move and separate from one another as the adjacent solid elements deform. The relative normal and tangential tractions for the two-dimensional cohesive elements are calculated at the element integration points according to the traction separation law defined by Eq. (2). The element has two integration points, corresponding to those of the QUAD2D element. The parameters associated with the cohesive element definition in ABAQUS are the number of nodes for the element and their connectivity, the cohesive zone parameters associated with the element, and the solution-dependent state variables required for the element. Figure 4 shows a TBC finite element model with cohesive elements along a representative crack path.

## 4. PARAMETRIC MODELING OF CRACK INITIATION AND PROPAGATION IN THE TOP COAT

The parametric space is defined by parameter ranges given in Table 2 and is spanned by nearly 100



**TABLE 2.** Range of variation of parameters from experimental observations reported in [2,7,32–35]

Parameter	Range of Variation
TGO thickness ( $h$ ) ( $\mu\text{m}$ )	2–6
Undulation amplitude ( $A$ ) ( $\mu\text{m}$ )	5–50
Undulation wavelength ( $W$ ) ( $\mu\text{m}$ )	10–160
TC thermal expansion ( $a_{\text{TC}}$ )	$6\text{--}12 \times 10^{-6}$
TGO thermal expansion ( $a_{\text{TGO}}$ )	$4\text{--}8 \times 10^{-6}$
Top coat modulus ( $E_{\text{TC}}$ ) (GPa)	100–220
TGO modulus ( $E_{\text{TGO}}$ ) (GPa)	320–400

simulations. These results yield information about how crack initiation and extension in the TBC system is sensitive to important geometrical, material, and loading parameters. Critical analysis of the results demonstrates that there are some parameter ranges that provide safer TBC designs.

TBC failure due to top coat spallation can be characterized by crack initiation and crack propagation phases. Two studies are conducted to investigate these phases. These studies are performed sequentially, namely, the probable locations of crack initiation are determined in the first study, and the subsequent study assumes existence of a finite crack at that location.

#### 4.1 Sensitivity Analysis for Crack Initiation within the Top Coat

To identify the critical parameters assisting crack initiation, a sensitivity analysis of the maximum first principal stress ( $S1^{\text{max}}$ ) with respect to geometric, material, and loading parameters is performed for the TBC system. Candidate parameters considered in the sensitivity analysis are (1)  $h$ , thickness of the TGO; (2)  $A$ , amplitude of the sinusoidal undulation; (3)  $W$ , wavelength of the undulation; (4)  $t$ , thickness of the top coat; (5)  $E_{\text{TGO}}$  and  $a_{\text{TGO}}$ , stiffness and thermal expansion coefficient of the TGO; (6)  $E_{\text{TC}}$  and  $a_{\text{TC}}$ , stiffness and thermal expansion coefficient of the top coat; (7)  $s_r$ ,  $s_h$ , and  $s_c$ , heating, hold and cooling time of the thermal cycle, respectively; and (8)  $T_{\text{peak}}$ , peak temperature of the thermal cycle load. Definitions of the geometric parameters are pictorially given in Fig. 2. Individual parameters are varied incrementally, while keeping all others stationary; that is, parametric variation is achieved by changing the value of one parameter at

a time. This is needed to isolate the effect of each parameter on the damage initiation and propagation. Such variation is performed for each parameter until the entire parametric space is spanned.

The simulations revealed that the magnitude and location of  $S1^{\text{max}}$  in the top coat is sensitive to several parameters. It also shows that  $S1^{\text{max}}$  occurs either along the axis of symmetry or along the interface. Hence the location of the  $S1^{\text{max}}$  is characterized by its normal distance from the interface ( $v$ ). A representative set of the sensitivity analyses results for  $S1^{\text{max}}$  magnitude are summarized in Figs. 5(a)–5(c), where the normalized  $S1^{\text{max}}$  is plotted as a function of the normalized geometric, material, and loading parameters, respectively. The  $S1^{\text{max}}$  for each plot is normalized by  $S1_0^{\text{max}}$ , the maximum among all reported results in that plot. Each parameter is normalized with its maximum value considered in this work.  $S1^{\text{max}}$  is found to be insensitive to any increase in the top coat thickness  $t$  or the bond coat thickness  $b$  beyond the nominal values ( $b = 60 \mu\text{m}$  and  $t = 100 \mu\text{m}$ ) selected. Figure 5a shows that principal stress decreases exponentially with increasing undulation wavelength  $W$  and asymptotically approaches zero. This is confirmed by the fact that an undulation with infinite wavelength corresponds to a flat interface, for which the  $S1^{\text{max}}$  principal stress is zero. For increasing amplitude  $A$ , there is first an increase in the principle stress and then exponential decay. Finally, the principal stress increases nonlinearly with the TGO thickness  $h$  and with quasi-stabilization at high thickness values.

Figure 5b shows that  $S1^{\text{max}}$  increases linearly with the top coat and TGO modulus, with the TGO modulus having a steeper increase. The principal stress decreases almost linearly with an increase in the thermal expansion coefficient of the TGO. How-

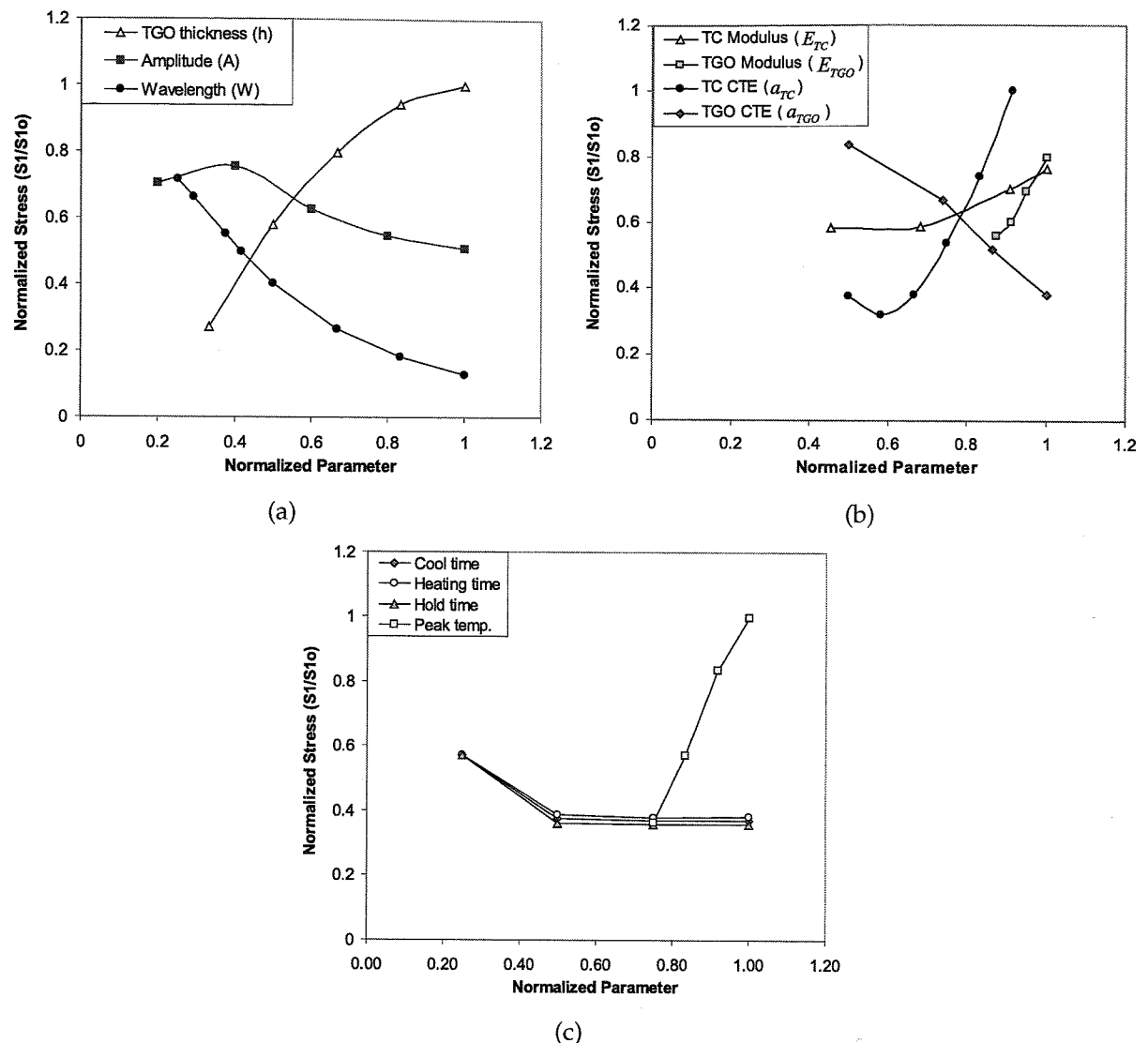


**FIGURE 5.** Plots showing top coat principal stress sensitivity to (a) geometric parameters (normalizing values of  $h^{\max} = 6 \mu\text{m}$ ,  $A^{\max} = 25 \mu\text{m}$ ,  $W^{\max} = 120 \mu\text{m}$ , and  $S_{10}^{\max} = 604 \text{ MPa}$ ), (b) material parameters (normalizing values of  $E_{TGO}^{\max} = 400 \text{ GPa}$ ,  $E_{TC}^{\max} = 220 \text{ GPa}$ ,  $\alpha_{TC}^{\max} = 12\text{e-}6$ ,  $\alpha_{TGO}^{\max} = 8\text{e-}6$ , and  $S_{10}^{\max} = 167.16 \text{ MPa}$ ), and (c) thermal load cycle parameters (normalizing values of  $s_r^{\max} = 40 \text{ min}$ ,  $s_c^{\max} = 40 \text{ min}$ ,  $s_h^{\max} = 40 \text{ min}$ ,  $T_{\text{peak}}^{\max} = 1200^\circ\text{C}$ , and  $S_{10}^{\max} = 363.20 \text{ MPa}$ )

ever, increasing the thermal expansion coefficient of the top coat first decreases the principal stress and then causes rapid increase.

Figure 5c shows that the increase in peak temperature of the thermal cycle almost linearly increases the principal stress. For a higher values, the duration of the cooling and holding do not influence the principal stress. However, significant decreases in

the cooling and holding durations can increase the principal stress significantly.

Parametric sensitivities of normal distance ( $v$ ) of the  $S_1^{\max}$  location from the interface are summarized in Figs. 6(a)–6(c), where the normalized  $v$  is plotted as a function of the normalized geometric, material, and loading parameters. The  $v$  for each case are normalized with respect to the correspond-

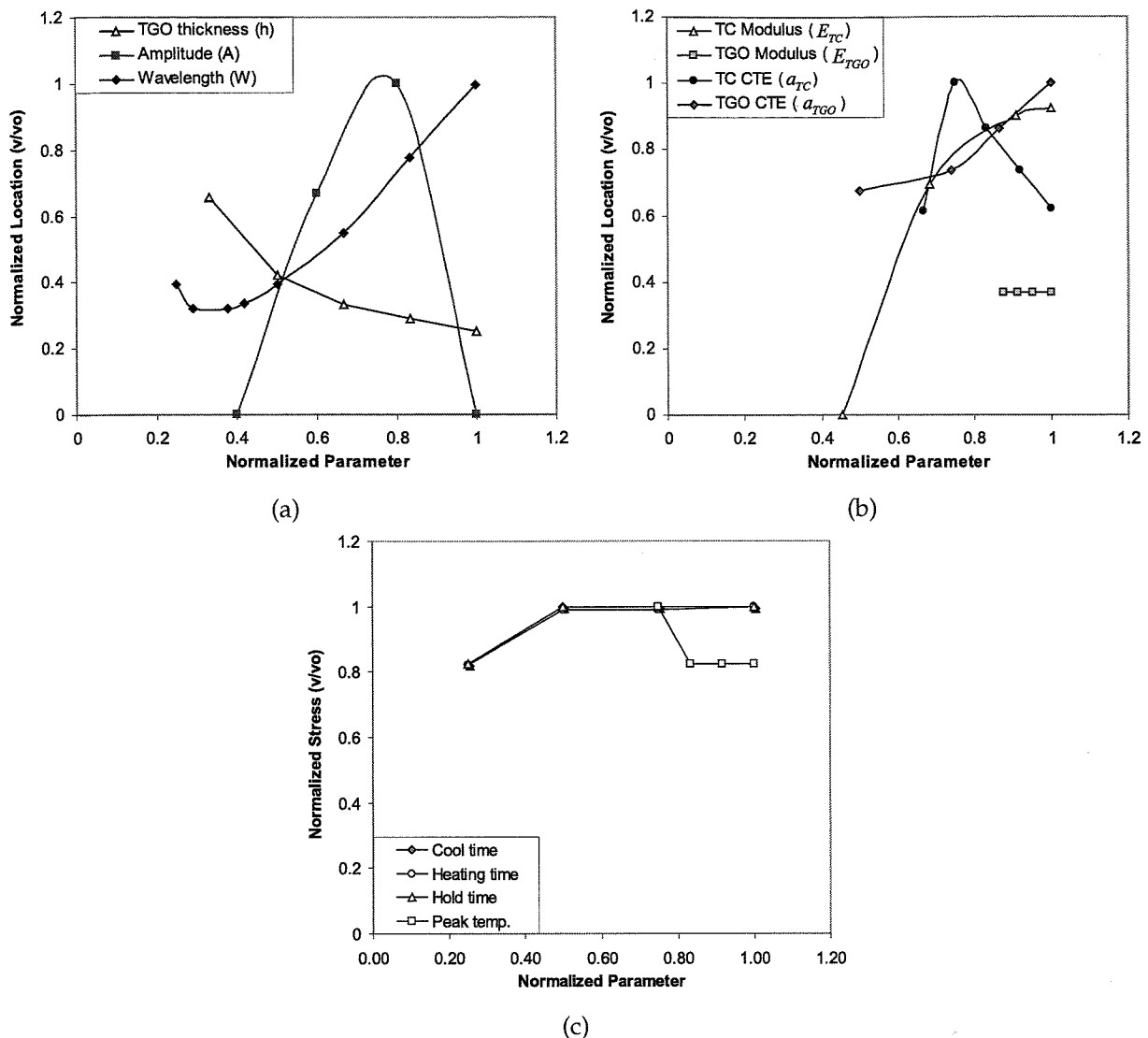


**FIGURE 6.** Plots showing sensitivity of the location of principal stress to (a) geometric parameters (normalizing values of  $h^{\max} = 6 \mu\text{m}$ ,  $A^{\max} = 25 \mu\text{m}$ ,  $W^{\max} = 120 \mu\text{m}$ , and  $v_0 = 15.22 \mu\text{m}$ ), (b) material parameters (normalizing values of  $E_{TGO}^{\max} = 400 \text{ GPa}$ ,  $E_{TC}^{\max} = 220 \text{ GPa}$ ,  $a_{TC}^{\max} = 12\text{e-}6$ ,  $a_{TGO}^{\max} = 8\text{e-}6$ , and  $v_0 = 32.53 \mu\text{m}$ ), and (c) thermal load cycle parameters (normalizing values of  $s_r^{\max} = 40 \text{ min}$ ,  $s_c^{\max} = 40 \text{ min}$ ,  $s_h^{\max} = 40 \text{ min}$ ,  $T_{\text{peak}}^{\max} = 1200^\circ\text{C}$ , and  $v_0 = 20.18 \mu\text{m}$ )

ing maximum value of normal distance  $v_0$ , and each parameter is normalized with respect to its maximum value reported in the figure captions. Figure 6a shows that increasing TGO thickness reduces the normal distance ( $v$ ) of  $S1^{\max}$  from the interface. An increase in wavelength first reduces  $v$  before sharply increasing it. The variation in  $v$  due to increase in amplitude is parabolic, with  $v$  increasing from zero, reaching a peak, and then reducing back

to zero. However, it should be noted that for these simulations, reduction of  $v$  to zero resulted from the  $S1^{\max}$  location moving to a different location along the interface and not just returning to the initial location.

Figure 6b shows that for their range of variation, the moduli of TGO and top coat do not influence the location  $v$ . An increase in TGO thermal expansion coefficient increases  $v$  exponentially. The rela-

tionship between  $v$  and  $a_{TC}$  is parabolic. Figure 6c shows that the location of  $S1^{\max}$  is insensitive to any increase in duration of heating, cooling, and holding time beyond 10 min. Furthermore, there is little change for a considerable increase in peak temperature.

#### 4.2 Parametric Domain Map for Damage Initiation in the Top Coat

The sensitivity analyses show that the maximum of the first principal stress ( $S1^{\max}$ ) magnitude as well as its normal distance from the interface ( $v$ ) is very sensitive to several parameters. Owing to the highly nonlinear response that results from bond coat creep and cyclic loading, closed form parametric equations to predict failure are infeasible. Instead, a domain-partitioning map of the critical geometric parameters is developed as a tool to predict TBC failure.

From the sensitivity analyses, TGO thickness and undulation geometry are found to emerge as geometric parameters that have the most effect on damage. The multidimensional parametric space spanned by the parameters  $h$ ,  $A$ , and  $W$  is characterized to predict failure. In this work, a novel reduced-order parametric space is introduced that can effectively represent the multiparameter dependence of damage initiation. Two nondimensional parameters ( $\psi$ ,  $\xi$ ) are uniquely defined from sensitivity and dimensional analysis for this representation as

$$\psi = \frac{h^2}{A \times W} \quad (17a)$$

$$\xi = \frac{W}{A} \left( \frac{h}{h_0} \right)^{\left( \frac{2A}{W} \right)^3} \quad (17b)$$

where  $h$  is the TGO thickness,  $A$  is the undulation amplitude,  $W$  is the undulation wavelength, and  $h_0 = 1 \mu\text{m}$ . Partitioning of the two-dimensional ( $\psi$ ,  $\xi$ ) domain delineates regions of different damage characteristics. Three distinct domains, viz. safe, fail, and subsafe subdomains, are introduced. The safe domain corresponds to the geometries for which no crack will be initiated in the top coat. The fail domain contains those geometries for which interfacial cracks will initiate. The subsafe domain corresponds to geometries for which cracks will initiate away from the interface and further loading will determine if they will propagate toward the

interface. The boundaries of the three distinct domains are delineated by critical nondimensional parameters  $\psi_c$  and  $\xi_c$ , and the domains are expressed as

$$\begin{aligned} \text{Fail domain:} & \quad \psi \geq \psi_c \text{ \& } \xi \geq \xi_c \\ \text{Subsafe domain:} & \quad \psi \geq \psi_c \text{ \& } \xi < \xi_c \\ \text{Safe domain:} & \quad \psi < \psi_c \end{aligned} \quad (18)$$

The critical values ( $\psi_c$ ,  $\xi_c$ ) are evaluated in the following steps:

1. Conduct simulations for various combinations of parameters and designate each parametric combination as fail, safe, or subsafe based on results of crack initiation.
2. Determine the corresponding parameters ( $\psi$ ,  $\xi$ ) from Eq. (17). The critical values  $\psi_c$  and  $\xi_c$  are identified as those that correspond to the transition between the different fail-safe domains, as shown in Fig. 7.

The critical coordinates defining the partition boundaries are determined to be  $\psi_c = 2.0 \times 10^{-2}$  and  $\xi_c = 4.8$ . It should be noted that this domain delineation is done for  $E_{TC} = 200 \text{ GPa}$

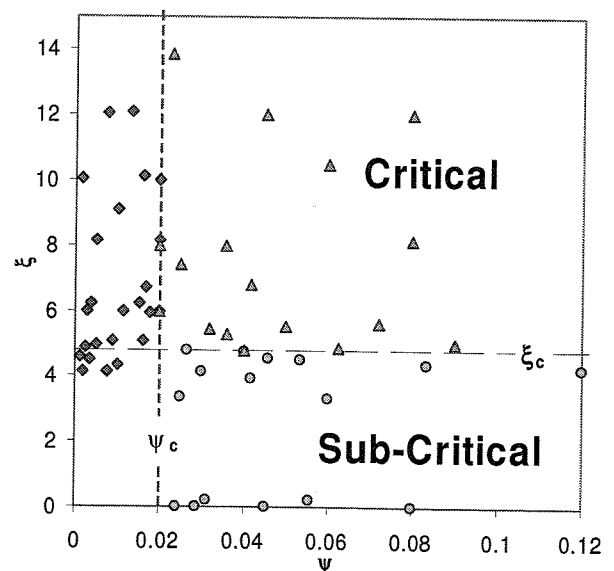


FIGURE 7. Plot showing the domain map of the parametric space delineating TBC designs into safe, subsafe, and fail combinations based on two unique combinations of parameters  $\psi$  and  $\xi$

and  $E_{TGO} = 400$  GPa. The complete dependence of these domains on  $E_{TC}$  and  $E_{TGO}$  will be explored in a future article.

#### 4.3 Sensitivity Analysis for Crack Propagation within the Top Coat

For the domain map, the safe configurations that do not initiate cracks and the fail configurations that initiate cracks at the interface are readily identified. However, the occurrences of subsafe configurations require additional analysis for further subdivision into safe and fail. Since the maximum principal stress axis is always parallel to the axis of symmetry, a horizontal crack path is selected for all subsafe geometries and is laced with hysteretic cohesive elements. The crack is allowed to propagate with cyclic thermal loading while monitoring the incremental direction of propagation. As discussed in Section 2.2.2, the analysis is terminated when the incremental direction of crack propagation ( $\alpha_0$ ) exceeds 0.1% of the critical angle ( $\alpha_c$ ).

The cracks that deviate away from the interface ( $\alpha_0 > 0$ ) at the termination of the analysis are unlikely to cause interfacial delamination and are thus reclassified as safe. Configurations that propagate cracks toward the interface ( $\alpha_0 < 0$ ) could reach the interface and become fail or could arrest and become safe. Given the complexity of the cracks propagating toward the interface, the present focus is on cracks that are repelled away from the interface.

A parametric investigation of the sensitivity of the incremental direction with geometric parameters including (1)  $h$ , thickness of the TGO; (2)  $A$ , amplitude of the sinusoidal undulation; and (3)  $W$ , wavelength of the undulation. Figure 8 shows the relationship between crack propagation direction ( $\alpha_0$ ) normalized by its maximum value and normalized geometric parameters. Each parameter is normalized with the maximum value given in the figure caption. Figures 8 shows that increase in TGO thickness ( $h$ ) decreases the incremental angle ( $\alpha_0$ ), which promotes potentially critical cracks that are attracted toward the interface. An increase in undulation amplitude ( $A$ ) or wavelength ( $W$ ) is likely to suppress critical cracks as they promote repulsion of cracks away from the interface.

The functional dependence of crack deflection on geometric parameters is formalized using the following dimensionless parametric expression  $\zeta$ :

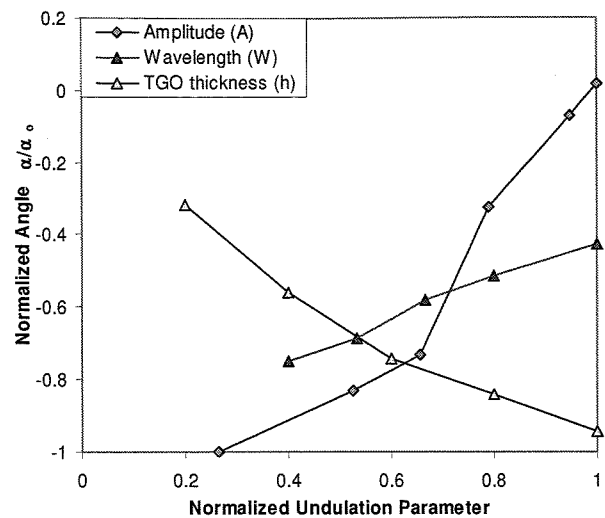


FIGURE 8. Plot showing sensitivity of the incremental direction of crack propagation to geometric parameters (normalizing values of  $h^{\max} = 10 \mu\text{m}$ ,  $A^{\max} = 38 \mu\text{m}$ ,  $W^{\max} = 120 \mu\text{m}$ , and  $\alpha_0 = 8.73^\circ$ )

$$\zeta = \frac{A}{A_0} \frac{W}{h} \cos \left( 2\pi \frac{h}{h_0} \right) \quad (19)$$

where  $A$  is the undulation amplitude,  $W$  is the undulation wavelength, and  $h$  is the TGO thickness;  $h_0 = 5 \mu\text{m}$  and  $A_0 = 10 \mu\text{m}$ . Sensitivity studies show that for the subsafe parametric combinations for which  $\zeta \leq \zeta_c$ , the cracks are repelled away from interface and are deemed safe. The critical value,  $\zeta_c$ , is determined from the sensitivity data to be 2.32. Similar to the domain map, this delineation of safe geometries is done for  $E_{TC} = 200$  GPa and  $E_{TGO} = 400$  GPa. This parametric expression  $\zeta$  can be used in combination with domain maps for selection of safer TBC designs.

#### 5. COMPARISON OF NUMERICAL PREDICTION WITH EXPERIMENTS

As a final step, the experimental observations of top coat failure are reported in the literature [2,6] are compared with the domain map prediction as well as finite element simulations. Two cases are considered for which geometric parameters and crack trajectories are obtained from SEM micrographs, as follows:

- $A = 10 \mu\text{m}$ ,  $W = 40 \mu\text{m}$ , and  $h = 3 \mu\text{m}$ , with a crack initiating at  $v \sim 9 \mu\text{m}$  and propagat-



ing horizontally for  $\sim 14 \mu\text{m}$  before deviating sharply toward the interface and leading to delamination (Fig. 8(b) in [2]).

- b.  $A = 10 \mu\text{m}$ ,  $W = 30 \mu\text{m}$ , and  $h = 3 \mu\text{m}$ , with a crack initiating at  $v \sim 5.5 \mu\text{m}$  and propagating horizontally for  $\sim 7.5 \mu\text{m}$  before deviating toward the interface and penetrating the TGO layer (Fig. 7(c) in [7]).

For both cases of  $A$ ,  $W$ , and  $h$  parameter combinations in the two situations described above, Eq. (18) predicts the TBC to be in the subsafe domain. This is in agreement with the experimentally observed crack initiation away from the interface.

The finite element simulations with nominal values for material and cohesive parameters (i.e.,  $E_{\text{TGO}} = 400 \text{ GPa}$ ,  $E_{\text{TC}} = 200 \text{ GPa}$ , and  $\sigma_{\text{max}} = 287 \text{ MPa}$ ) yield the following crack trajectories for the corresponding cases described above:

- a. The crack initiates at  $v = 9.8 \mu\text{m}$  from the interface and propagates horizontally for  $15 \mu\text{m}$  before the first directional update.
- b. The crack initiates at  $v = 6.38 \mu\text{m}$  from the interface and propagates horizontally for  $8.75 \mu\text{m}$  before the first directional update.

In both cases, the cracks deviate toward the interface, indicating a possibly critical crack. The finite element simulations of crack initiation and propagation agree very well with the experimentally observed crack trajectories. This implies that the modeling framework employed to develop the domain map is capable of accurately predicting crack trajectories.

## 6. CONCLUSIONS

In this article, failure characteristics of elastic top coats for TBCs are investigated using a finite element model. The evolution of maximum principal stress determines the onset of top coat cracking. Some of these cracks are postulated to subsequently lead to delamination of the interface between the top coat and the TGO. A hysteretic cohesive zone model is employed to study crack propagation within the top coat. The materials and geometries in the study are chosen to be representative of TBC materials in real applications. The contribution of geometric parameters to crack initiation is estimated, and a multidimensional parametric space

is represented as a reduced-order two-dimensional parametric domain map for crack initiation in terms of the parameters. The reduced-order domain map is constructed by collecting the relevant parameters into two unique variables that span the two-dimensional domain. This domain classifies the design space as fail, safe, and subsafe for crack initiation.

The direction of crack propagation for TBC designs identified as subsafe is also investigated. The crack propagation is assumed to be in the direction that maximizes the cohesive energy based on the criterion proposed by Li and Ghosh [16]. Since interfacial delamination is ultimately responsible for TBC failure, designs that attract the crack toward the interface are deemed fail, and those repelling it are deemed safe. The potentially safer combinations within the subsafe domain are identified by a third dimensionless expression within the domain map. However, this domain map is limited to specific material properties of the constituent layers, and explicit dependence on material parameters will be established in a subsequent articles.

The article concludes with finite element simulations of two representative failure scenarios from the literature. The geometry and material properties for these cases are obtained from the literature, and nominal material properties are selected for simulations. The parametric domain map predictions for criticality of crack initiation and propagation are found to be in good agreement with experimental observations. Furthermore, finite element simulations of the propagation also compare well with the experimentally observed crack trajectories.

Despite establishing parametric criteria to determine initiation of microcracks in the top coat, the present study is limited to establishing the critical direction of crack propagation. However, cracks that tend to propagate *toward* the interface do not ensure interfacial delamination since the crack may arrest before actually reaching the interface. Thus the proposed domain maps provide a conservative estimate of safer TBC designs. Parametric investigations accounting for other factors like rate of crack propagation can reduce the conservativeness and are the subject of future work.

## ACKNOWLEDGMENTS

The authors are grateful for the support provided by the National Aeronautics and Space Administration (NASA) through a University Research Engineering Technology Institute (URETI) grant to the Ohio State University for Aeropropulsion and Power Technology (UAPT). Computer support by the Ohio Supercomputer Center through grant PAS813-2 is also gratefully acknowledged.

## REFERENCES

1. Wright, P. K., and Evans, A. G., Mechanisms governing the performance of thermal barrier coatings. *Curr. Opin. Solid State Mater. Sci.* **4**:255–265, 1999.
2. Spitsberg, I. T., Mumm, D. R., and Evans, A. G., On the failure mechanisms of thermal barrier coatings with diffusion aluminide bond coatings. *Mater. Sci. Eng. A.* **394**:176–191, 2005.
3. Kim, H., Investigation of critical issues in thermal barrier coating durability. PhD thesis, Ohio State University, Columbus, 2005.
4. Tolpygo, V. K., Clarke, D. R., and Murphy, K. S., Evaluation of interface degradation during cyclic oxidation of EB-PVD thermal barrier coatings and correlation with TGO luminescence. *Surf. Coatings Technol.* **188**:62–70, 2004.
5. Vaidyanathan, K., Gell, M., and Jordan, E., Mechanisms of spallation of electron beam physical vapor deposited thermal barrier coatings with and without platinum aluminide bond coat ridges. *Surf. Coatings Technol.* **133**:28–34, 2000.
6. He, M. Y., Evans, A. G., and Hutchinson, J. W., Effects of morphology on the decohesion of compressed thin films. *Mater. Sci. Eng. A.* **245**:168–181, 1998.
7. Evans, A. G., Mumm, D. R., Hutchinson, J. W., Meier, G. H., and Pettit, F. S., Mechanisms controlling the durability of thermal barrier coatings. *Prog. Mater. Sci.* **46**:505–553, 2001.
8. Evans, A. G., Hutchinson, J. W., and He, M. Y., Micromechanics model for the detachment of residually compressed brittle films and coatings. *Acta Mater.* **47**:1513–1522, 1999.
9. Bhatnagar, H., Ghosh, S., and Walter, M. E., Parametric studies of failure mechanisms in elastic EB-PVD thermal barrier coatings using FEM. *Int. J. Solids Struct.* **43**:4384–4406, 2006.
10. Xu, T., He, M. Y., and Evans, A. G., A numerical assessment of the propagation and coalescence of delamination cracks in thermal barrier systems. *Interface Sci.* **11**:349–358, 2003.
11. Karlsson, A. M., Xu, T., and Evans, A. G., The effect of the thermal barrier coating on the displacement instability in thermal barrier systems. *Acta Mater.* **50**:1211–1218, 2002.
12. Karlsson, A. M., Hutchinson, J. W., and Evans, A. G., The displacement of the thermally grown oxide in thermal barrier systems upon temperature cycling. *Mater. Sci. Eng. A.* **351**:244–257, 2003.
13. Xu, T., He, M. Y., and Evans, A. G., A numerical assessment of the durability of thermal barrier systems that fail by ratcheting of the thermally grown oxide. *Acta Mater.* **51**:3807–3820, 2003.
14. Anderson, T. L., *Fracture Mechanics: Fundamentals and Applications*. 2nd ed. CRC Press, Boca Raton, FL, 282–289, 1995.
15. Camacho, G. T., and Ortiz, M., Computational modeling of impact damage in brittle materials. *Int. J. Solids Struct.* **33**:2899–2938, 1996.
16. Li, S. H., and Ghosh, S., Multiple cohesive crack growth in brittle materials by the extended Voronoi cell finite element model. *Int. J. Fract.* **141**:373–393, 2006.
17. Ortiz, M., and Pandolfi, A., Finite-deformation irreversible cohesive elements for three-dimensional crack-propagation analysis. *Int. J. Numer. Methods Eng.* **44**:1267–1282, 1999.
18. Swaminathan, S., Pagano, N. J., and Ghosh, S., Analysis of interfacial debonding in three-dimensional composite microstructures. *J. Eng. Mater. Technol.* **128**:96–106, 2006.
19. Xu, X. P., and Needleman, A., Numerical simulations of fast crack-growth in brittle solids. *J. Mech. Phys. Solids.* **42**:1397–1407, 1994.
20. Nguyen, O., Repetto, E. A., Ortiz, M., and Radovitzky, R. A., A cohesive model of fatigue crack growth. *Int. J. Fract.* **110**:351–369, 2001.
21. Maiti, S., and Geubelle, P. H., A cohesive model for fatigue failure of polymers. *Eng. Fract. Mech.* **72**:691–708, 2005.

22. Erdogan, F., and Sih, G. C., On the crack extension in plates under plane loading and transverse shear. *J. Basic Eng.* **85**:519–527, 1963.
23. Palaniswamy, K. K. W. G., On the problem of crack extension in brittle solids under general loading. *Mech. Today.* **4**:87–148, 1978.
24. Sih, G. C., Strain energy density factor applied to mixed mode crack problem. *Int. J. Fract.* **10**:305–321, 1974.
25. Pan, D., Chen, M. W., Wright, P. K., and Hemker, K. J., Evolution of a diffusion aluminide bond coat for thermal barrier coatings during thermal cycling. *Acta Mater.* **51**:2205–2217, 2003.
26. ABAQUS. *User's Manual*. Hibbit, Karlsson and Sorrensen, Pawtucket, RI, 2005.
27. Balint, D. S., and Hutchinson, J. W., An analytical model of rumpling in thermal barrier coatings. *J. Mech. Phys. Solids.* **53**:949–973, 2005.
28. Johnson, C. A., Ruud, J. A., Bruce, R., and Wortman, D., Relationships between residual stress, microstructure and mechanical properties of electron beam physical vapor deposition thermal barrier coatings. *Surf. Coatings Technol.* **109**:80–85, 1998.
29. Zhu, D. M., Miller, R. A., Nagaraj, B. A., and Bruce, R. W., Thermal conductivity of EB-PVD thermal barrier coatings evaluated by a steady-state laser heat flow technique. *Surf. Coatings Technol.* **138**:1–8, 2001.
30. Cheng, J., Jordan, E. H., Barber, B., and Gell, M., Thermal/residual stress in an electron beam physical vapor deposited thermal barrier coating system. *Acta Mater.* **46**:5839–5850, 1998.
31. Adams, J. W., Ruh, R., and Mazdidasni, K. S., Young's modulus, flexural strength, and fracture of Yttria-stabilized Zirconia versus temperature. *J. Am. Ceramic Soc.* **80**:903–908, 1997.
32. Choi, S. R., Hutchinson, J. W., and Evans, A. G., Delamination of multilayer thermal barrier coatings. *Mech. Mater.* **31**:431–447, 1999.
33. Gell, M., Vaidyanathan, K., Barber, B., Cheng, J., and Jordan, E., Mechanism of spallation in platinum aluminide/electron beam physical vapor-deposited thermal barrier coatings. *Metall. Mater. Trans. A.* **30**:427–435, 1999.
34. Mumm, D. R., Evans, A. G., and Spitsberg, I. T., Characterization of a cyclic displacement instability for a thermally grown oxide in a thermal barrier system. *Acta Mater.* **49**:2329–2340, 2001.
35. Tolpygo, V. K., and Clarke, D. R., Surface rumpling of a (Ni, Pt) Al bond coat induced by cyclic oxidation. *Acta Mater.* **48**:3283–3293, 2000.